Weighted sum optimization for combined thermoelectric geometry and electric pulse using finite elements

J.L. Pérez–Aparicio[a], P. Moreno–Navarro[a], J.J. Gómez-Hernández[b]

[a]Department of Continuum Mechanics & Theory of Structures, Universitat Politècnica de València, Spain
[b]Research Institute of Water and Environmental Engineering, Universitat Politècnica de València, Spain

Abstract

Thermoelectric materials assembled in Peltier cells are an increasingly widespread option for generating electricity from residual sources and refrigeration, even at the nanoscale. These cells can cool below the nominal temperatures with an electric pulse, during short periods and for applications such as laser devices or microchips. The present article uses heuristic algorithms to improve the response of a Peltier cell by concurrently optimizing the pulse and geometry of its thermoelements. The study is based on the Finite Element method, handling full coupling and dynamics of the thermal, electric, and mechanical fields and temperature dependency of the material properties. The optimization algorithm is Simulated Annealing, capable of discarding local minima to reach robust results and permitting set limiting factors such as the maximum stress. The main novelty lies in multilayered geometries and pulse shapes that can reproduce any geometry and pulse virtually. First, a complete parametric analysis under constant pulse is presented to understand the complexities of the temperature, electric flux, and stress distributions in these layered geometries. Second, combined optimizations are discussed. The targets are overcooling temperature, time to reach it, overheating minimization, overcooling duration, and combinations. In the best cases, the first target is doubled, the second is reduced to a few milliseconds, the third is null, and the duration can be 95% of the pulse while reducing the stress up to 40%.

Keywords: Multiphysics dynamics, nonlinear finite element, simulated annealing, weighted sum–multiparameter, thermoelement optimization, thermoelectric pulse optimization, mechanical stress failure

Nomenclature

I	Electric current	A
T	Temperature	°C
l	TE (or layer) length	m
A	TE cross–sectional area	m^2
ρ	Mass density	kg/m^3
c_p	Specific heat	J/kg K
α_T	Thermal expansion coefficient	1/K
λ, μ	Lamé's parameters	Pa
α	Seebeck coefficient	V/K
κ	Thermal conductivity	W/K m
γ	Electric conductivity	A/V m
Q	Thermal power	W
x	Spatial coordinates	m
$\boldsymbol{j}$	Electric flux	A/m^2
V	Electric potential	V
$\boldsymbol{q}$	Thermal flux	W/m^2

$\boldsymbol{\sigma}$	Stress tensor	Pa
C	Stiffness tensor	Pa
$\boldsymbol{\varepsilon}$	Strain tensor	–
$\boldsymbol{\beta}$	Thermal stress tensor	Pa/K
$\boldsymbol{u}$	Displacement vector	m
c	TE layer width	m
e	TE depth	m
P	Pulse gain	–
t	Time	s
ξ	Dimensionless coordinate	–
ϕ	Area ratio	–
d_1	TE vertical slope	–
σ	Normal stress	Pa
τ	Tangential stress	Pa
O	Objective function	–
φ	Weighting coefficient	–
m	Target value	°C, s
s	Target standard deviation	°C, s
θ	Annealing "temperature"	–
i	Iteration counter	–

Sub–, Super–scripts

⁻	Prescribed property, average
op	Optimal
h	Hot side
c	Cold side
css	Cold face at steady state
$1, 2, 3$	Spatial direction
i, j, k	Component, counter
ad	Admissible
˙	1st time derivative
p	Pulse
pp	Post–pulse
mx	Maximum
ht	Holding time
mn	Minimum
0	Reference, origin
VM	Von Mises
˜	Perturbed

Acronyms

TE	Thermoelectric
TC	Thermocouple
FE	Finite Element
COP	Coefficient–of–Performance
BC	Boundary Condition
SA	Simulated Annealing

1. Introduction

Peltier cells, due to their low material cost, ease of use, and applicability across a range of scenarios, from cooling isolated systems without moving parts to micro-scale sensors and actuators, have garnered significant attention. Achieving optimal performance in these devices hinges on calculating an electric intensity $\bar{I}_{op}$ that maximizes the *Peltier* effect while minimizing the *Joule* effect, a relationship expressed in Eq. (3). During steady-state operation, the *Peltier* effect prevails over the *Joule* heat and *Fourier* conduction effects to maintain cooling at the cold face.

Sophisticated applications, such as lasers and electronic circuits, necessitate additional cooling during brief transient periods, often referred to as "overcooling". This involves temporarily increasing I beyond $\bar{I}_{op}$ to enhance the *Peltier* effect, albeit at the expense of increased *Joule* heat. The challenge lies in ensuring that *Joule* heat does not compromise cooling performance during overcooling, which requires a deep understanding of the transient state.

The transient state of Peltier cells is inherently challenging to study due to the intricate interplay of coupled phenomena, dynamics, and the delicate balance between the *Peltier*, *Joule*, and *Fourier* effects. Moreover,

as local temperature differences increase during over-cooling, phenomena like the *Thomson* effect, which accounts for variations in TE properties with temperature, become more pronounced. Additionally, the transient state imposes heightened thermomechanical stresses, demanding robust TE designs.

Recent articles [1] and [2] reviewed the state–of–the–art in Peltier cells for refrigerating electronic circuits, highlighting the need for research in areas such as contacts, integration, manufacturing processes, new materials, and design optimization. It is this last aspect that our paper addresses.

Historically, constant section parallelepipeds were favored due to their ease of manufacture. However, advancements in nanoscale technology, exemplified in [3], have enabled the production of more intricate shapes at a competitive cost. Thin film depositions of TEs for cooling electronic devices [4] and innovative cooling garments [5] exemplify this trend.

The optimization of TE geometries for steady-state applications has been explored in depth. Notable reviews [6] have scrutinized the impact of TE dimensions, layers or TC cell distribution. Also, optimization algorithms on the performance, both for cooling and power generation applications (see [7] or [8]). However, these studies often focus on simple geometrical variations, neglecting the effect of transversal area variation.

However, the review lacked coverage of TE geometry optimization involving variations in transversal area, as observed in works such as [9], [10], and [11]. These studies conducted parametric analyses to identify optimal shapes for various objectives, studying basic linear transversal area variations. Additionally, advanced optimization algorithms were used in the works of [12], [7], and [13], to explore unconventional shapes and designs. Recent contributions in this field (see [14], [4], and [15]) further underscore the evolving landscape of TE geometry optimization.

In this paper, a novel approach to optimizing pulsed Peltier cells is presented. The method revolves around the innovative design for TE geometries and electric pulses utilizing a piecewise approach. The focus is on adjusting the width of specific points within the TE structure and optimizing gain values at specific times, employing interpolation for intermediate values. This optimization technique enables precise fine–tuning of parameters, leading to substantial performance enhancements for pulsed Peltier cells.

In addition to addressing the complexity of TE geometry optimization, the present study considers the often-neglected Thomson effect and electrical contact resistance. Recent work [8] underscores the significance of

the *Thomson*, which can lead to a 7% difference in the results. Also, for miniaturized TEs, electrical contact resistance cannot be ignored, further emphasizing the need for a comprehensive analysis.

While many previous studies rely on commercial codes for their analyses, these tools often impose limitations on material model complexity. Many previous studies rely on commercial codes for their analyses. While commercial codes offer advantages, such as ease of use and widespread availability, they often have inherent limitations on material model complexity. Consequently, these limitations can impede the flexibility and customization required to address the nuances of the thermoelectric formulation. In contrast, we employ a comprehensive nonlinear FE code—introduced in [16], [17], and [18]—integrated with the research FE software FEAP [19] from UC Berkeley. This code effectively couples mechanical, electric, and thermal fields, accounting for T–dependent properties.

To identify optimal geometries, which may be intricate and counterintuitive, a heuristic algorithm previously applied to optimize electric pulses is applied [20]. This same approach guides our work in optimizing TE geometries, offering a robust and adaptable methodology.

This paper is structured as follows: Section 2 provides a brief description of the models, followed by a parametric study of predetermined geometries in Section 3. SA is the selected optimization procedure [21] introduced in Section 4, highlighting its ability to handle complex objectives and nonlinear optimization problems. Finally, Sections 5 and 6 delve into intricate geometries and optimization results, significantly enhancing performance.

2. Description of the model

In the Peltier cell studied in the current article, only one of the 128 TCs is considered (see the representation of the complete Peltier cell in [22]). In addition, only a quarter of the TC is meshed due to symmetries, representing only half of a p–doped TE as shown in Figure 1. With these simplifications, the distributions of T and V and the absolute values of the fluxes and stresses are the same in the two TEs if their α are equal [23] in absolute value.

Figure 1 illustrates four distinct materials stacked from bottom to top. Starting from the outermost, Al_2O_3 can be seen, followed by $SnPb$, Cu, and finally the layered Bi_2Te_3. It is important to note that among these materials, only Bi_2Te_3 possesses thermoelectric properties within the cell. The thermoelectric BCs are a pre-
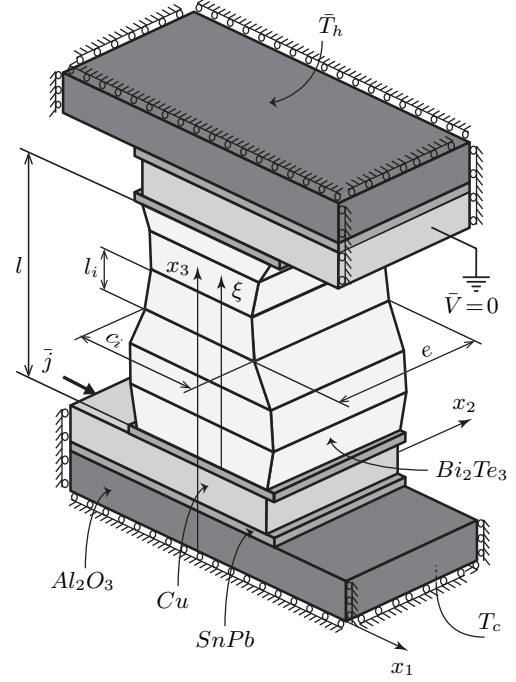

Figure 1: Half–thermocouple with mechanical hinges at hot and cold faces and repetition at left and right as in [22]; layered thermoelement with variable area. Overbars denote prescribed magnitudes.

scribed optimal electric current $\bar{j}_{op}$ proportional to $\bar{I}_{op}$. A particular interface FE developed in [22] is used for this purpose. Also, $\bar{T}_h = 50°C$ is set at the top face, and V is gauged to zero at the top Cu cut. The bottom T_c can take any value, but its thermal flux is forced to $Q_c = 0$ W. The material properties used throughout the calculations are listed in Table 1.

The repetition and symmetry cuts define the mechanical BCs, and hinged surfaces are considered of the several possible conditions at the Al_2O_3 hot and cold faces. Since the Peltier cells often are encapsulated, convection and radiation through internal air are neglected, and TE contacts are considered perfect.

Although T will be reported in *Celsius* degrees, *Kelvin* degrees are considered in the equations. The current formulation governs the TE coupled with mechanical phenomena, and it is based on the constitutive (first column) and equilibrium (second column) equations:

$$\boldsymbol{j} = -\gamma \nabla V - \alpha \gamma \nabla T; \qquad \nabla \cdot \boldsymbol{j} = 0$$

$$\boldsymbol{q} = -\kappa \nabla T + \alpha T \boldsymbol{j}; \qquad \rho c_p \dot{T} = -\nabla \cdot \boldsymbol{q} - \boldsymbol{j} \cdot \nabla V$$

$$\boldsymbol{\sigma} = \boldsymbol{C} : \boldsymbol{\varepsilon} - \boldsymbol{\beta}\,(T - T_0); \qquad \rho \ddot{\boldsymbol{u}} = \nabla \cdot \boldsymbol{\sigma}$$
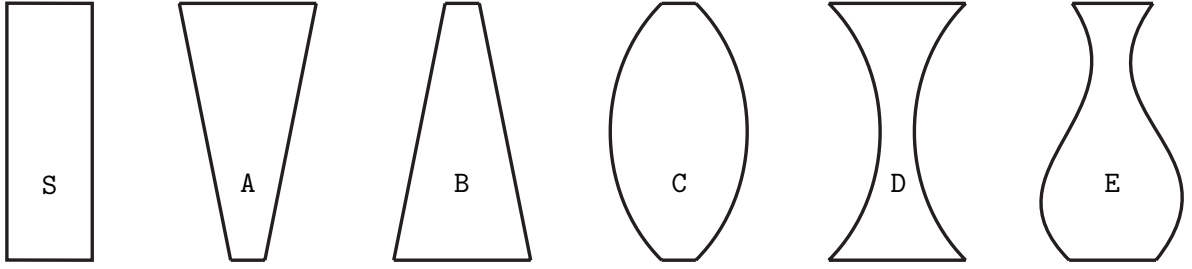
$$\tag{1}$$

Figure 2: Geometries of thermoelements for transient parametric study with cold face at the bottom and hot face at the top: constant "straight" S, linear "pyramids" A and B, quadratic "barrel" C, "hourglass" D, cubic "vase" E.

	Al_2O_3	Cu	$SnPb$	Bi_2Te_3
$\rho \times 10^3$	3.57	8.96	7.31	7.53
$c_p \times 10^2$	8.37	3.85	2.26	5.44
$\alpha_T \times 10^{-6}$	5.0	17	27	16.8
$\lambda \times 10^{10}$	16.34	7.16	3.25	6.71
$\mu \times 10^{10}$	15.08	4.39	1.68	1.68
κ	35.3	386	48	$\kappa(T)$
$\gamma \times 10^6$	0	58.1	4.72	$\gamma(T)$
α	0	0	0	$\alpha(T)$
$\sigma_{ad} \times 10^6$	–	–	–	60

Table 1: Properties of the Peltier cell materials of Figure 1 from [24]. Temperature–dependent properties of Bi_2Te_3 from polynomials of [25]; typical allowable stress from [26].

The TE widths c_i of Figure 1 vary piecewise, but the thickness e in direction x_2 is constant; this is a limiting condition that could easily be overcome but facilitates the construction of the FE mesh. Otherwise, and thanks to this layered shape, there are no restrictions on the geometries the optimization algorithm can handle. However, maximum and minimum widths will be imposed to avoid singular figures.

The study [20] demonstrated that only the mechanical field is significantly influenced by the mesh size, while convergence can be achieved in the electric and thermal fields even with coarse meshes. To optimize the simulation time, given the large number of cases the optimization algorithm will handle, a convergence study was conducted to determine the minimum element size required for satisfactory results.

The mesh consists of 27-node hexahedra isoparametric elements. Figure 3 shows the results for the number of elements in the x_3 direction for shape E (refer to Figure 2) and $l = 0.006$ m. It is important to note that the number of elements must be a multiple of the number of layers. Based on the findings, it can be concluded

that a minimum of 24 elements and a maximum of 40 are sufficient for obtaining a reliable estimation of stress in the thermoelement, corresponding to an element size ranging from 0.15 to 0.25 mm.
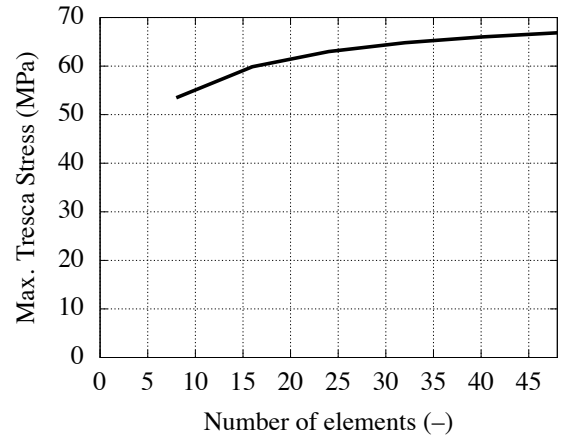

Figure 3: Maximum Von Mises stress for a different number of elements in direction x_3.

For each iterated TE geometry, it is necessary to find the $\bar{I}_{op}$ that maximizes Q_{css} so that a steady state minimum T_{css} can be achieved. Optimal intensities have been obtained in the past, but in general, for parallelepipedal (straight) or linear TEs, viz. [24] or [27]. Since this work aims to determine optimal geometries of a variable section, a semi–analytical procedure for a general $\bar{I}_{op}$ is taken from [25] to avoid additional time–consuming FE runs. Although very fast, this calculation is recursive since each layer of Figure 1 is under constant but different T; that is, $\alpha(T)$, $\gamma(T)$, $\kappa(T)$ are variable along l. The fitted polynomials for the three

properties are from [24]:

$$\alpha = 1.988{\times}10^{-4} + 3.353{\times}10^{-7}\,T + 7.52{\times}10^{-10}\,T^2$$

$$\kappa = 1.663 - 3.58{\times}10^{-3}\,T + 3.195{\times}10^{-5}\,T^2$$

$$\gamma = 1.096{\times}10^5 - 5.59{\times}10^2\,T + 2.498\,T^2 \tag{2}$$

3. Parametric study in transient state

This section presents a parametric study of the TE basic geometries sketched in Figure 2, keeping the dimensions and shapes of the other material parts from Figure 1. The linear geometries have been extensively studied in the literature, and the rest in [25]. Still, the following results' novelty lies in the electric prescription's dynamic nature.

For comparison purposes, all lengths are fixed at $l = 5$ mm, and the maximum 1.5 mm and minimum 0.75 mm widths are equal for all variable geometries, except an average of 1 mm for the straight S.

The steady state is driven by $\bar{I}_{op}$, producing a cold face temperature T_{css}. Suddenly, a step pulse of constant gain $P = 2.5$ and duration $t_p = 6$ s is applied; see Figure 4(a) and (b): the overcooling starts, and the cold face eventually achieves its minimum $T_{css} - \Delta T_p$. When the extra volumetric heat due to *Joule* reaches this cold face by conduction, the temperature increases up to $T_{css} + \Delta T_{pp}$ at t_{mx}. Without other pulses, T slowly returns to the steady state level for a long time (out of the figure) due to the evacuation of the extra heat through the hot face. The holding time t_{ht} (or "uptime") is the period for which the overcooling is at least 80% of the maximum ΔT_p.

The resulting T_c evolutions during the transient state calculated with FEAP are plotted in Figure 4(c). Since all TEs are subjected to the same pulse, the initial slopes are equal since it mostly depends on the equal l. It already can be observed that the best–performing geometry to achieve the largest ΔT_p (the most crucial target) is E.

By order of importance, the three main causes of this good overcooling are:

a1) Due to *Joule*, the maximum T_{mx} appears in the neck far away from the cold face, then its influence on T_c is delayed.

a2) From [20], the prescribed dynamic intensity $P \cdot \bar{I}_{op}$ is among the lowest, producing a reduced *Joule*.

a3) The area is the largest by the cold face, allowing an efficient *Peltier* evacuation of heat despite a cold face smaller than the maximum.

Geometry B fulfills a1 even better than E, but not the other two causes; A and D are, for this target, the worst geometries since they only partially comply with the three causes. For C, the maximum *Joule* will be generated at both ends. Still, because of a3 (or equivalently because of the large volume at the barrel center), the TE can evacuate from the cold face, an essential part of the heat by *Peltier*.

The overheating ΔT_{pp} is minimum for B and E due to two causes:

b1) The T_c at pulse removal are among the lowest since they achieve excellent ΔT_p and good t_{ht}.

b2) The volumes of their bottom halves are the largest, then the *Joule* that arrives at the cold face is smaller for the same pulse energy.

The S and D geometries also perform well due to both b1 and b2 and their ability to externally evacuate heat quickly, partly thanks to their sizeable hot face sections.

The holding time t_{ht} is optimal again with B and E because of a1. The significant heat conduction in the TE middle also helps maximize t_{ht} for E. Also, C presents a good result, but E is better due to its smaller cold face area.

As a summary, the B, C, and E geometries are appropriate for most targets except for t_{mn}. Whereas both A and D are undesirable due to the generation of large *Joule* heat near the cold face, the significant difference between them is their maximum mechanical stress, to be studied next. The straight S gives intermediate but poor results for most targets.

The spatial T distributions during steady state calculated with FEAP are shown in Figure 5(a). As for the repetitive optimization cases, the FE mesh is relatively coarse to minimize the running time but does not produce a loss of precision; see [20] for a convergence study of the same mesh and thermoelectric case. The horizontal variation of T is negligible. Still, the vertical variation is significant, provoking vertical free expansion in the top half of the TE and contraction in the rest, especially near the cold face. The expansion is maximum near the neck, where T reaches its highest 53.2°C; the TE remains at $T_0 = 20$°C in the middle, and the cooling is −30.7°C near the lower end. Due to these differences and combined expansion and contraction, the whole TE tends to move toward the bottom.
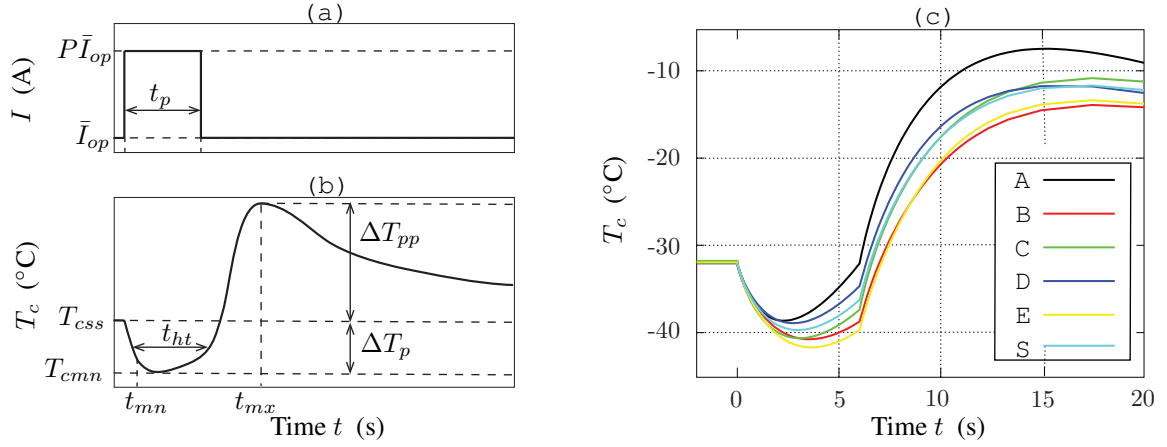
5

Figure 4: Transient cold face temperature for Figure 2 geometries computed by the Finite Element method under temperature–dependent properties.
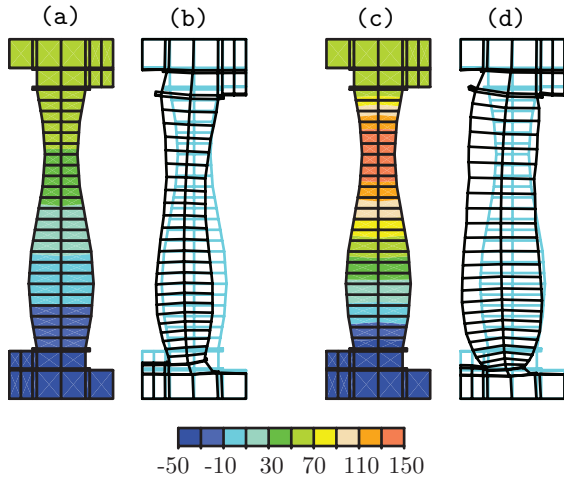

Figure 5: Contour plot temperatures in °C and deformation at steady state, (a) and (b), and at transient state at maximum cold face temperature, (c) and (d), for E from Figure 2. Initial (blue), deformed ×400 (black line) meshes.

Figure 5(b) shows the deformed geometry of E also in steady state. The distortions are primarily due to two related causes: (i) compression/expansion due to decrement/increment of T with respect to T_0 and (ii) bending due to the rotation of the TE ends. The latter answers to the difference of α_τ between Cu and Al_2O_3 (the last very low, see Table 1), combined with the mechanical and repetition BCs of Figure 1. The $SnPb$ solder has a minimum thickness of 0.05 mm and does not significantly influence deformations.

Figures 5(c) and 5(d) show identical distributions but

at t_p (pulse removal) when the highest stresses appear due to the accumulated electric energy introduced. The cold face reaches $T_{cmn} = -39$°C, significantly lower than the steady state -30.7°C. The trade–off is that at this instant, T_{mx} jumps to 145°C by the neck, almost three times the steady maximum 53°C. Consequently, 5/6 of the TE is now above T_0, tending to expand in all directions much more than during steady state. Due to the general augmentation of T, most TE also tries to expand vertically. Still, the Al_2O_3 restriction prevents it, producing the corresponding stress increase and stress–induced stiffness which reduces the rotation of the TE ends.

The T distributions of Figures 5(a) and 5(c) (and of the other geometries of Figure 2) are essential for understanding the final shapes that SA will produce. Other relevant issues are the adiabatic nature of the cold face and the constant pulse.

For further interpretation, consider the simplified 1D model deduced from [25] for geometrical linear variation at steady state and under constant properties:

$$q(\xi) = I\alpha \, \frac{\bar{T}_h \ln \phi_{0\xi} - T_c \ln \phi_{l\xi}}{\ln \phi_{0l}} +$$
$$\frac{d_1 \kappa}{\ln \phi_{0\xi}} \left(T_c - \bar{T}_h \right) - \frac{I^2}{d_1 \gamma} \ln \left(\phi_{0\xi} \phi_{l\xi} \right) ;$$

$$\phi_{0\xi} := \frac{A(0)}{A(\xi)} ; \qquad \phi_{0l} := \frac{A(0)}{A(l)} ; \qquad \phi_{l\xi} := \frac{A(l)}{A(\xi)}$$

(3)

where the coordinate ξ is defined in Figure 1 and $A(0)$, $A(l)$ the cold an hot faces' areas.

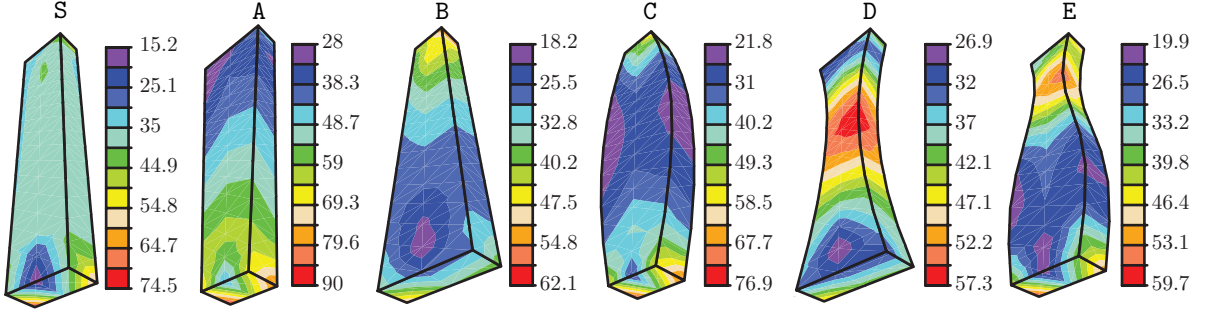The *Peltier* effect (first term of the right–hand side) is

6

Figure 6: Contour plots for Von Mises stress in MPa for the thermoelement geometries of Figure 2 at pulse removal t_p defined in Figure 4(a). Computations are performed using three–dimensional coupled and dynamic finite elements.

essential during the pulse application due to the increment of the intensity I, especially in or near the possible necks that SA will predict. The *Fourier* conduction and *Joule* generation (second and third terms) modify the flux depending on: i) the sign of the T distribution and ii) the variable area $A(\xi)$, respectively.

In the modeled p–doped TE of Figure 1, the heat flux is upward in most of the TE from the pulse beginning to when ΔT_p (maximum cooling) is reached. However, from this instant to t_{mx}, the flux is upward in the upper part and downward in the lower part. Then, there is an intermediate zone with zero flux—not necessarily in the middle—a function of many parameters: l, t_p, BCs, and significantly the geometry. Finally, after t_{mx}, the steady state slowly recovers, and the flux is upward again.

One of the important contributions of the present work is the analysis of mechanical stresses, which can reach very high values in transient states for some geometries and pulses. Figure 6 shows contour plots of the Von Mises equivalent stresses σ_{VM} in the TE at pulse removal.

The treatment of the mechanical field in Eq. (1) is linear elastic. Therefore possible stress relaxations can occur due to plasticity in Cu and $SnPb$ or to damage in the stiff and brittle Al_2O_3. Despite this simplification, the observed trends are correct since high stresses are restricted to small zones. The components of σ_{VM} come from:

c1) The high vertical stress σ_{x_3}, due to the vertical mechanical constriction.

c2) The small but influential shear stresses $\tau_{x_1x_3}$, $\tau_{x_2x_3}$ due to the α_T mismatch and rotations.

During the transient process, c1 and c2 can happen simultaneously at some TE points leading to stress concentrations. The first candidate for these concentrations
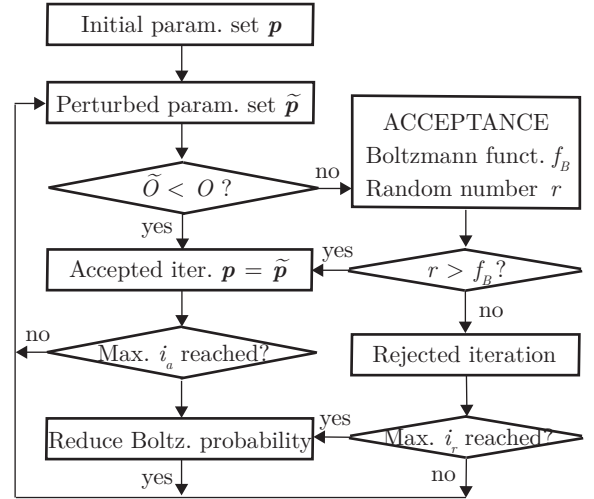

Figure 7: Simulated Annealing optimization algorithm flow chart.

is the TE corners close to the cold face, where a high T increment occurs.

The σ_{VM} highest values and their locations are different for each geometry, demonstrating the importance of the mechanical analysis. With σ_{ad} from Table 1 and analyzing Figures 6, it can be concluded that while for B, D, and E, the maxima are about the permissible, for the other geometries they are much higher; for A, the excess is a significant 50%, with a poor overcooling performance.

As commented, the necks are concentrators of *Joule* heat, and, as long as they do not lie close to the cold face, their existence favors the TE mechanical performance since they can decouple the stress causes, as in B, D, and E. The neck should be in the top half since the $\bar{T}_h = 50°C$ BC reduces the T increment, and the maximum *Joule* heat takes longer to reach the cold face. The

comparison between A and C is paradigmatic: the small cold face section provokes high stresses in both, but for C, they are lower due to $a3$. The slightly higher stress in the cold face of E compared with that of D can also be attributed to the smaller cold face area of the former. In Figure 6, it is clear that the stress distributions of D and E are not only proportional to thermomechanical strains $\beta[T(\xi)-T_0]$ but also, indirectly through the third Eq. (1), to the bending drawn in Figures 5(b) and 5(d).

4. Simulated Annealing

SA is a heuristic optimization method that mimics the metallurgical process of heating and controlled cooling, known as annealing, to get an optimal crystallization of a metallic material. SA is used to solve global optimization problems in large search spaces, which can involve multiple and potentially conflicting targets.

The objective function O to be minimized is a weighted sum of each target function. Before the optimization begins, several evaluations of each target function are calculated to find their average value and standard deviations. Then, the function takes the form of the left expression:

$$O(\boldsymbol{p}) = \sum_{k=1}^{4} \varphi_k \, \frac{m_k(\boldsymbol{p}) - \bar{m}_k}{s_k} \; ; \qquad f_B = \exp\left(\frac{\Delta O}{\theta}\right) \quad (4)$$

where $1 \leq k \leq 4$ since four targets will be analyzed. SA aims to find the $\boldsymbol{p}$ that minimizes $O(\boldsymbol{p})$; each new parameter vector is proposed by taking previous values from suitable prior distributions.

The target values are computed for a given parameter set, and O is evaluated. Then, one of the parameters, chosen at random, is perturbed by drawing a new value from its distribution. The O is reevaluated, and a decision is taken: if the new function $\tilde{O}$ is better than the previous one, the new parameter value is accepted. If not, a random choice is made whereby a parameter value that does not improve O will be accepted with a probability that it will be prominent in the initial iterations i but decrease as the iterations increase. The probability is given by a Boltzmann's distribution function of the right Eq. (4), where $\Delta O = \tilde{O} - O$ is the (negative) change in the objective function. Notice that the TE T is unrelated to the annealing θ, which should decrease as the optimization iterations progress. The higher θ, the more likely an unfavorable proposal will be accepted. There must be a cooling schedule specifying after how many iterations θ should go down and by which factor. This possibility of accepting unfavorable proposals prevents

SA from being trapped in a local minimum, making it a global optimization method.

Figure 7 shows a flow diagram of the algorithm. The first iteration counter i_a counts the number of accepted parameter vectors: when i_a reaches a maximum value, θ is reduced, and this counter is reset to zero. The second i_r counts the number of rejected vectors $\boldsymbol{p}$: again, when i_r reaches a maximum value, θ is reduced, and this counter is reset to zero. When there are three resets of i_r, the optimization process stops.

Parameter	Symbol	Min.	Max.
Layer widths	c_i	0.75	1.5
TE length	l	2.5	7.0
Pulse duration **I**	t_p	2.1	10
Pulse duration **II**	t_p	2.1	11.2
Pulse gain	P_j	1	6

Table 2: Input parameters and their intervals for the optimizations.

Each input parameter's minimum and maximum allowed values are taken from uniform distributions of the intervals indicated in Table 2. The TE geometry is parametrized using the layer widths c_i drawn in Figure 1 and the total TE length l. Eight layers are considered, assigning c_1 to the layer close to the cold face $\xi = 0$ and c_9 close to the hot face $\xi = l$. The pulse is parameterized using eight pulse gains P_j equally spaced during the pulse duration t_p as in Figure 8. The resulting pulse shapes are smoothed using cubic Hermite interpolation polynomials. The pulse always ends with a constant $P = 1$, and eventually, stabilization is reached.

The pulse duration t_p must be within limits to avoid introducing insufficient or excessive electric energy in the device. Notice that two different t_p maxima depend on the optimization type described below. The widths c_i are also taken from the indicated interval to avoid impractical geometries. During the optimization, l and the TE geometry are the most critical parameters since, as explained before, they control the time *Joule* heat takes to reach the cold face by conduction.

Two different optimizations, to be presented in Sections 5 and 6, are run depending on the input parameters to optimize:

I *Geometry*. Input parameters: $\{c_i, \ i = 1, \ldots, 8\}$, l, and t_p. The pulse is constant $P = 2$.

II *Pulse + Geometry*. Input parameters: $\{c_i, \ i = 1, \ldots, 8\}$, l, t_p, and $\{P_j, \ j = 1, \ldots, 8\}$.

For each optimization, six different cases will be studied: the first four optimize the targets shown in Figure 4(b):
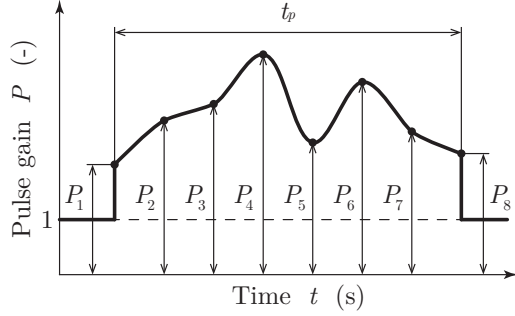
8

Figure 8: Sketch of a pulse introduced to the Simulated Annealing optimization algorithm.

- C1: maximization of overcooling ΔT_p

- C2: minimization of t_{mn} to reach 80% of ΔT_p

- C3: minimization of overheating ΔT_{pp} after t_p

- C4: maximization of holding time t_{ht}

An essential feature of the current SA is setting a limit for the maximum stress allowed in the TE, taken as σ_{ad} from Table 1. The reason to define t_{mn} as 80% of the maximum overcooling is because, with **II**, more than one T_c local minima could appear. The other two cases combine objectives:

- C5: simultaneous optimization of C1, C2, C3, C4

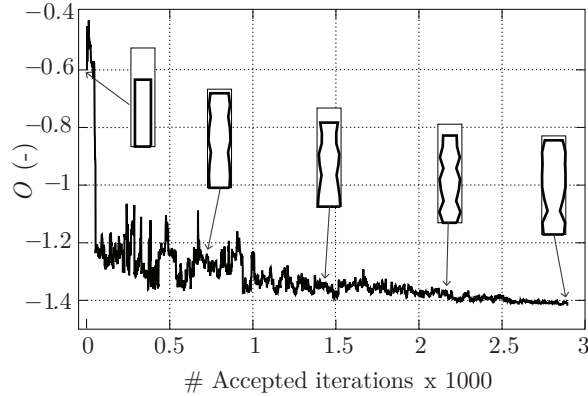- C6: simultaneous optimization of C1, C3, C4

Figure 9: For case C4, accepted iterations versus objective function; thermoelectric geometry calculated evolution.

Figure 9 shows the evolution of O with accepted iterations for optimization **I** and case C4. The TE geometry has been drawn at five different iterations. The

progression is not monotonic since SA can get momentarily trapped in local minima.

The FE and SA models are run with a computer with a CPU Intel–Core i7-4930K (12 cores) and 64 Gb of RAM in a Linux environment. Each FE example is executed in a single core mode, taking from 100 to 500 s, depending on the pulse duration. The SA algorithm typically needs about 6,000 iterations to converge for optimization **I** and more than 10,000 for **II**.

5. Optimized geometries under constant pulse

In this section, the optimization of only TE geometries for the cases defined in Section 4 is determined using the FE and SA models previously described. Table 3 presents interesting results, with $\bar{I}_{op}$ corresponding to the best iteration. Variable geometries can maintain σ_{VM} much below σ_{ad}, except for C2 due to the high electric energy introduced already during steady state by its high $\bar{I}_{op}$.

Figure 10 displays the final geometries of the six cases (top row) and the calculated T_c evolutions (bottom row). Cases C3 and C6 that optimize ΔT_{pp} have a similar bottleneck near the hot face, causing the *Joule* heat to concentrate around it and leading to a T–gradient that facilitates heat evacuation. This behavior was observed in Figure 5(c) with T jumping from 145°C to 50°C.

C1, which maximizes ΔT_p exclusively, gives an optimal geometry similar to the preliminary E from Figure 2. The highest allowed l and c_i prevent *Joule* heating and its conduction. The overcooling is 10°C, an improvement from 7.7°C of Figure 4(c) for E, and in addition, the calculated $\sigma_{VM} \approx 30$ MPa is a significant reduction from the 50.7 MPa of S.

Case	$\bar{I}_{op}$	t_p	l	σ_{VM}
C1	0.9	8.0	6.9	29.6
C2	2.55	2.1	2.5	57.9
C3	0.7	2.1	7.0	31.8
C4	1.0	10	6.7	43.7
C5	1.33	6.8	5.5	46.6
C6	0.86	9.9	7.0	30.6

Table 3: Thermoelement geometry optimization **I**. Steady state intensity and optimized: pulse duration, length, and maximum von Mises stress.

The only optimized parameter in case C2 is t_{mn}, resulting in a geometry that achieves a concise t_{mn} with a small ΔT_p. This geometry favors the arrival of *Joule* to the cold face, resulting in shorts l and t_p, a neck, and an
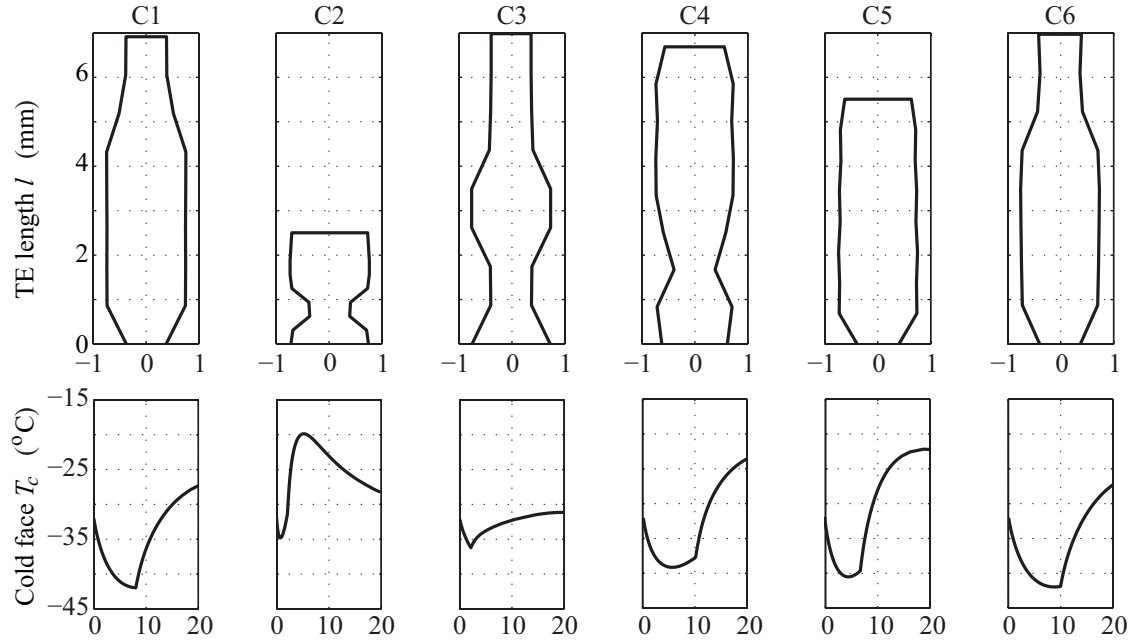
9

Figure 10: Optimized thermoelement geometries (first row, in abscissa centered width in mm) and resulting cold face temperature evolution (bottom row, in abscissa time in s).

area expansion near the cold face. The resulting geometry is similar to D but with a rectangle at the top and a very short effective length $l = 1.25$ mm. The neck is not directly assigned to the cold face because creating heat is more efficient if this neck is located at a section with a high T at steady state. The SA algorithm limits the obtained stress level to 58 MPa; a geometry similar to A would give better t_{mn}, but the stresses would have been too high. The intense heat generated has its drawback in the high ΔT_{pp} after the pulse. Minimizing only C2 goes against the general TE dynamic improvement since the best way to reduce t_{mn} is the absence of ΔT_p, but this case is used as a benchmark of SA optimization.

C3 minimizes ΔT_{pp}, requiring the suppression of *Joule* as much as possible: l is selected as the maximum allowed and t_p as the minimum. The resulting geometry combines D and B with exponential variation, favoring a modest ΔT_p of 4.1°C and a corresponding very small ΔT_{pp} of 0.7°C.

Case C4 maintains a significant holding time by balancing the three flux components of Eq. (3) at the cold face. This balance is achieved by forcing a high T with a neck close to the cold face and a large cold face area to minimize *Joule* and favor conduction. The rest of the TE is almost straight, and l is nearly the largest, keeping $T_{mx} = 75$°C near the hot face and far from the cold face.

In C5, l is close to the maximum allowed, with a medium pulse duration of 6.8 s. This geometry optimizes t_{mn} and requires new evacuation systems since T_{mx} is closer to the hot face, and $A(l)$ is almost the allowed maximum.

The optimization cases C1, C5, and C6 aim to minimize ΔT_p and increase cold face area while reducing heat conduction within the TE. The area increase occurs in only one layer. In contrast, C2 and C3 have a bottleneck near the cold face, leading to modest ΔT_p values.

Based on the T_c evolutions of the lower Figure 10, it is shown that except for C4 and C5, which target t_{ht}, the pulse tends to end when the maximum overcooling is reached.

All single target cases (C1 to C4) demonstrate significant optimized improvements concerning S under similar conditions, with a notable decrease in the O indicating better results. However, compromises are necessary for combined cases such as C5 and C6 due to target contradictions, resulting in less noticeable individual increases.

6. Combined geometry and pulse optimization

Some targets of the previous section are more sensitive to pulse shape than TE geometry. Therefore, the
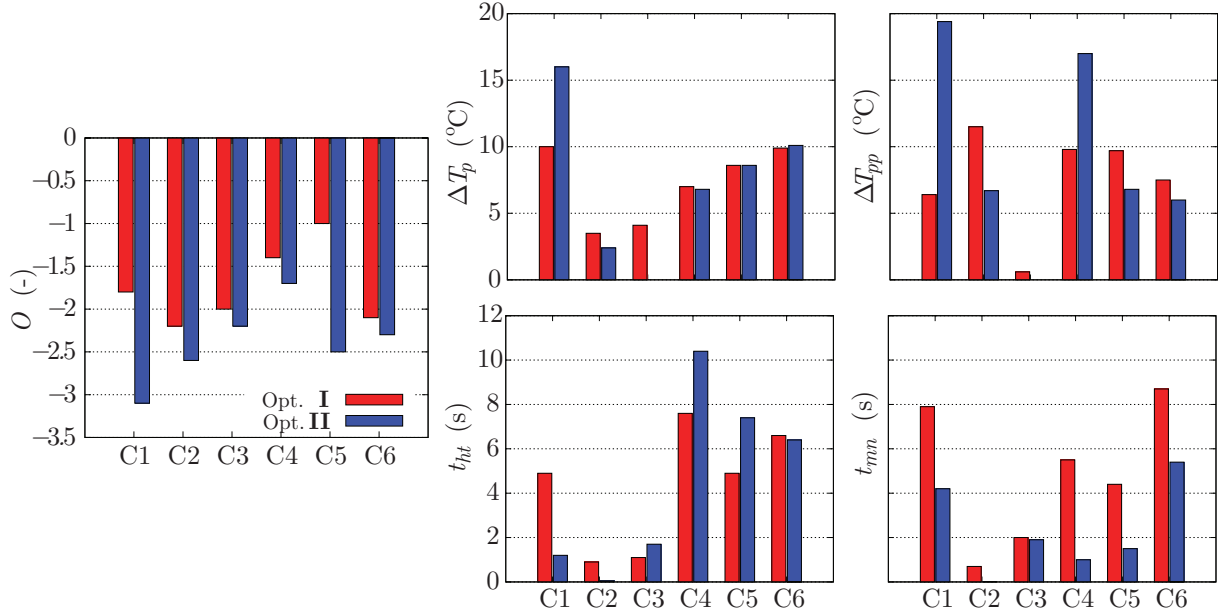
Figure 11: For the six cases and the two optimizations from Figures 10 and 12: left graphic, objective function; other graphics, the four calculated targets.

combined optimization **II** can yield interesting results without increasing stress levels.

Table 4 displays the SA results, including the maximum pulse gain of Figure 8. The new pulse limits allow for high or low electric energy, causing stress levels to increase or decrease. The other results are similar but for σ_{VM}. Except for case C2, the lengths of the optimized geometries are again almost the maximum because, with the 80% definition of t_{mn} of Section 4, there is no need to rush the arrival of *Joule* to the cold face. The bottlenecks above of C3 and C6 from Figure 10 and of E from Figure 2 are now obtained for all cases except for C2 and C4.

C1 exhibits a "saw" geometry in the upper part of the TE, but it only slightly improves ΔT_p and ΔT_{pp} compared to **I**. The resulting small perturbation at the end of the pulse only slightly changes the T_c evolution since it occurs after its minimum. The SA algorithm could have eliminated this perturbation with more iterations or a good tuning post–process, but the computing time was already too high.

In C2 and similarly to **I**, the goal is still to maximize *Joule*, which is achieved with the allowed maximum $P_1 \approx 6$ and a minimum l. With this high pulse gain, the same electric energy as in the previous section can be applied in less time, increasing the initial slope of T_c. The second pulse spike results from choosing the

lower limit $t_p = 2.1$ s without much influence on the target. The neck can now be directly on the cold face since the quadratically dependent *Joule* becomes much more critical than *Fourier* and *Peltier*.

Now that the pulse shape has been included in the optimization, C3 is not a case but a benchmark. The best pulse to avoid overheating is a zero pulse, $P_j = 0$. In this situation, any geometry will give zero ΔT_{pp}, so the result of the first row is only a possible solution with no specific meaning.

The C4 geometric solution is very similar to **I** in the TE lower part, but an additional neck appears in the upper part with minimum influence. The two pulse maxima induce two similar ΔT_p local minima. Although the second local minimum is absolute, the holding time t_{ht} starts at 1 s, and its optimal value is a significant 10.4 s, as shown in the last Figure 11.

The optimized pulses in Figure 12 second row are different from those of Figure 10 but similar to those in [20] for only pulse optimization, except C5 due to t_{mn} definition, suggesting pulse shape and TE geometry have independent effects. t_p tends to reach its maximum only when t_{ht} is present (C4, C5 and C6).

Figure 11 presents bar graphs summarizing the results of both optimizations. The outcomes are better for **II** than **I**; for example, the maximum ΔT_p is 16°C for the first and 10°C for the second. Optimization **I** has a
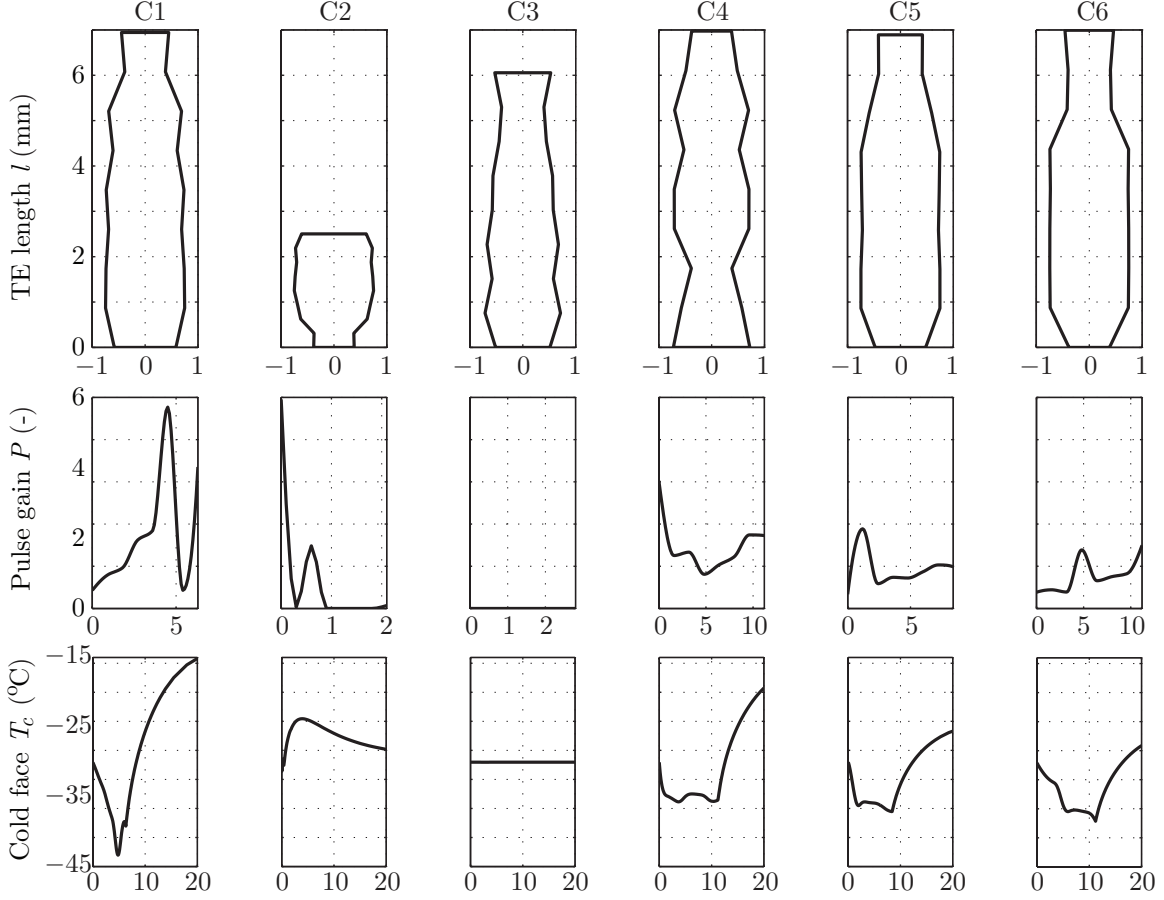
Figure 12: Combined optimized thermoelement geometries (first row, in abscissa centered width in mm) and pulse shape (second row, in abscissa time in s). Resulting cold face temperature evolution (bottom row, in abscissa time in s).

Case	$\bar{I}_{op}$	P_{mx}	t_p	l	σ_{VM}
C1	0.93	5.8	6.3	6.9	59.7
C2	2.61	5.9	2.1	2.5	59.5
C3	0.96	1.0	2.8	6.1	21.7
C4	0.84	4.0	11	7.0	48.2
C5	0.94	2.9	8.4	6.9	32.6
C6	0.88	2.5	11	7.0	29.2

Table 4: Thermoelement geometry plus pulse optimization **II**. Steady state intensity and optimized: maximum gain, pulse duration, length, and maximum von Mises stress.

low value for ΔT_{pp}, while **II** has a zero due to the lack of pulse, and almost the same is observed for t_{mn}. For t_{ht}, **II** achieves a 32% increase. Combined cases C5 and C6 offer less clear solutions due to compromises. While **II** cannot decrease ΔT_p, it can do so with ΔT_{pp} and t_{mn},

and only C5 increases t_{ht}. To better understand the effect of concurrently optimizing geometry and pulse, the left figure shows that the objective function significantly improves in all cases with **II**, particularly for C1 and C5, which are probably the most important cases.

Figure 13 shows the contours of the relevant magnitudes for the optimal geometry of C1 at the end of the applied pulse, $t = 6.3$ s. Due to the transverse area variation, isolines deviate from the perfect horizontal alignment expected in straight geometries. When the area increases, isolines tend to be concave, whereas when the area decreases, they tend to be convex.

The maximum T in the thermoelement is found near its top. The difference between the minimum and maximum values exceeds 160°C, which supports the requirement for variable properties in the thermoelement. Notably, the T–increase near the cold side is significantly greater than in the middle. V exhibits nearly linear vari-
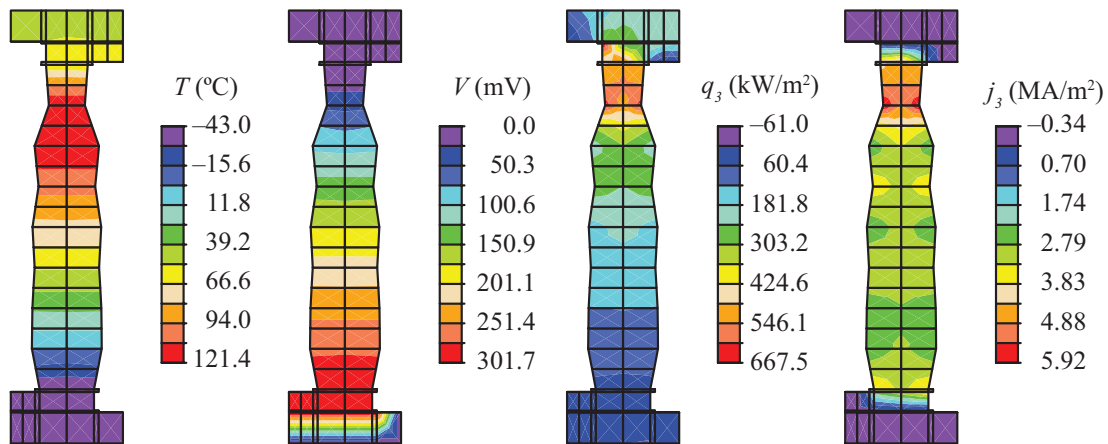
Figure 13: Contour plots of temperature, voltage, vertical heat flux, and vertical electric flux for the optimal geometry of Case 1 of Optimization **II** at the end of the pulse $t = 6.3$ s.

ation, although the rate of change tends to increase when the section decreases. The maximum V is directly associated with the applied pulse.

The fluxes, depicted in the last two figures, are correlated with the transverse area: as the area decreases, the flux increases, and vice versa. This relationship arises because the fluxes are measured per unit area, ensuring that the total integrated value remains constant across sections. The figures exclusively present the vertical component of the fluxes, which is the most relevant. Notably, most values are positive, indicating an upward direction.

7. Conclusions

The results of the current article show that at steady state, the thermoelement geometry does not significantly affect the temperature distributions, particularly near or at the cold face; in transient state, the distributions are heavily affected. Also, the geometry affects the *Joule* generation—concentrates this effect in necks— and the conduction but not the *Peltier* effect. Locating these necks close to the hot side is essential for many optimization targets.

Even if the geometry optimization alone does not improve the targets much, except for overcooling, it reduces the stresses significantly. This reduction is due to the different temperatures and heat flux distributions (the source of thermal stresses) when the geometry is nonregular.

With the boundary conditions considered in this work, it has been demonstrated that optimization can appreciably improve all targets if pulse shape and thermoelement piecewise geometry are simultaneously considered. The performance for some of these targets can be doubled, particularly the overcooling. The proposed methodology can develop custom–made solutions for general thermoelectric dynamic situations.

Acknowledgments

References

[1] Wen-Yi Chen, Xiao-Lei Shi, Jin Zou, and Zhi-Gang Chen. Thermoelectric coolers for on-chip thermal management: Materials, design, and optimization. *Materials Science and Engineering: R: Reports*, 151:100700, 2022.

[2] Zhi-Gang Chen and Wei-Di Liu. Thermoelectric coolers: Infinite potentials for finite localized microchip cooling. *Journal of Materials Science & Technology*, 121:256–262, 2022.

[3] Md Mofasser Mallick, Leonard Franke, Andres Georg Rösch, and Uli Lemmer. Shape-versatile 3d thermoelectric generators by additive manufacturing. *ACS Energy Letters*, 6(1):85–91, 2020.

[4] Tingrui Gong, Yongjia Wu, Juntao Li, Wenting Lin, Lei Gao, Limei Shen, Nan Zhou, and Tingzhen Ming. A system level optimization of on-chip thermoelectric cooling via taguchi-grey method. *Applied Thermal Engineering*, 214:118845, 2022.

[5] Yu Xu, Zijun Li, Junjian Wang, Mengsheng Zhang, Mintao Jia, and Qiaoli Wang. Man-portable cooling garment with cold liquid circulation based on thermoelectric refrigeration. *Applied Thermal Engineering*, 200:117730, 2022.

[6] S. Shittu, G. Lia, X. Zhao, and X. Ma. Review of thermoelectric geometry and structure optimization for t performance enhancement. *Applied Energy*, 268, 2020.

[7] Y.-X. Huang, X.-D. Wang, C.-H. Cheng, and David T.-W. Lin. Geometry optimization of thermoelectric coolers using simplified conjugate-gradient method. *Energy*, 59:689–697, 2013.

[8] T. Lu, X. Zhang, J. Zhang, P. Ning, Y. Li, and P. Niu. Multi-objective optimization of thermoelectric cooler using genetic algorithms. *AIP Advances*, 6:095105–1–095105–8, 2019.

[9] H. Lv, X.-D. Wang, T.-H. Wang, and C.-H. Cheng. Improvement of transient supercooling of thermoelectric coolers through variable semiconductor cross-section. *Applied Energy*, 164:501–508, 2016.

[10] Limei Shen, Wenshuai Zhang, Guanyu Liu, Zhilong Tu, Qingqing Lu, Huanxin Chen, and Qingjun Huang. Performance enhancement investigation of thermoelectric cooler with segmented configuration. *Applied Thermal Engineering*, 168:114852, 2020.

[11] S. Lin and J. Yu. Optimization of a trapezoid-type two-stage peltier couples for thermoelectric cooling applications. *International Journal of Refrigeration*, 65:103–110, 2016.

[12] A. Z. Sahin and B. S. Yilbas. The thermoelement as thermoelectric power generator: effect of leg geometry on the efficiency and power generation. *Energy Conversion and Management*, 65:26–32, 2013.

[13] Guiqiang Li, Samson Shittu, Xiaoli Ma, and Xudong Zhao. Comparative analysis of thermoelectric elements optimum geometry between photovoltaic-thermoelectric and solar thermoelectric. *Energy*, 171:599–610, 2019.

[14] Xiaoxing Han and Yaxiong Wang. Experimental investigation of the thermal performance of a novel split-type liquid-circulation thermoelectric cooling device. *Applied Thermal Engineering*, 194:117090, 2021.

[15] Y. Gao, C. Shia, and X. Wang. Numerical study on transient supercooling performance of annular thermoelectric cooler. *Applied Thermal Engineering*, 182, 2021.

[16] J.L. Pérez-Aparicio, R. Palma, and R.L. Taylor. Multiphysics and thermodynamic formulations for equilibrium and non-equilibrium interactions: non-linear finite elements applied to multi-coupled active materials. *Archives of Computational Methods in Engineering*, 23(3):535–583, 2016.

[17] R. Palma, J.L. Pérez-Aparicio, and R.L. Taylor. Non–linear finite element formulation applied to thermoelectric materials under hyperbolic heat conduction model. *Computer Methods in Applied Mechanics and Engineering*, 213:93–103, 2012.

[18] R. Palma, J.L. Pérez-Aparicio, and R. Bravo. Study of hysteretic photovoltaic behavior using the finite element method, extended thermodynamic and inverse models. *Energy Conversion and Management*, 65:557–563, 2013.

[19] R.L. Taylor and S. Govindjee. *FEAP A Finite Element Analysis Program: Programmer Manual*. University of California, Berkeley, 2010. http://www.ce.berkeley.edu/feap.

[20] P. Moreno-Navarro, J.L. Pérez-Aparicio, and J.J. Gómez-Hernández. Optimization of pulsed thermoelectric materials using simulated annealing and non-linear finite elements. *Applied Thermal Engineering*, 120:603–613, 2017.

[21] C.L. Deutsch and A.G. Journel. *Geostatistical Software Library and User's Guide*. Oxford University Press, 1998.

[22] J.L. Pérez-Aparicio, R. Palma, and R.L. Taylor. Finite element analysis and material sensitivity of Peltier thermoelectric cells coolers. *International Journal of Heat and Mass Transfer*, 55:1363–1374, 2012.

[23] J.L. Pérez-Aparicio, R. Palma, and R.L. Taylor. Finite element analysis and material sensitivity of Peltier thermoelectric cells coolers. *International Journal of Heat and Mass Transfer*, 55:1363–1374, 2012.

[24] David Michael Rowe. *CRC handbook of thermoelectrics*. CRC press, 2018.

[25] Pablo Moreno-Navarro, José L. Pérez-Aparicio, and J.J. Gómez-Hernández. Analytical and multicoupled methods for optimal steady-state thermoelectric solutions. *Coupled Systems Mechanics*, 11(2):151–166, 2022.

[26] Th. Clin, S. Turenne, D. Vasilevskiy, and R.A. Masut. Numerical simulation of the thermomechanical behavior of extruded bismuth telluride alloy module. *Journal of Electronic Materials*, 38(7):994–1001, 2009.

[27] J.L. Pérez-Aparicio, R. Palma, and P. Moreno-Navarro. Elasto-thermoelectric non-linear, fully coupled, and dynamic finite element analysis of pulsed thermoelectrics. *Applied Thermal Engineering*, 107:398–409, 2016.